



Single-crystal growth and magnetic phase diagram of the enantiopure crystal of NdPt₂BYoshiki J. Sato ^{1,2,*}, Fuminori Honda,² Arvind Maurya,² Yusei Shimizu ², Ai Nakamura,² Yoshiya Homma,² Dexin Li,² Yoshinori Haga,³ and Dai Aoki²¹Graduate School of Engineering, Tohoku University, Sendai 980-8577, Japan²Institute for Materials Research, Tohoku University, Oarai, Ibaraki 311-1313, Japan³Advanced Science Research Center, Japan Atomic Energy Agency, Tokai, Ibaraki 319-1195, Japan

(Received 12 November 2020; revised 6 February 2021; accepted 16 February 2021; published 15 March 2021)

We report on the enantiopure single-crystal growth using the Czochralski method and the magnetic properties of the Nd-based monoaxial chiral magnet NdPt₂B based on electrical resistivity, specific heat, and magnetization measurements. A peak in the magnetic susceptibility and a λ -type anomaly in the specific heat are observed at $T_{N1} = 19.5$ K. Successively, a first-order magnetic transition at $T_m = 9.5$ K is observed in the electrical resistivity, specific heat, and magnetic susceptibility. In addition, we observed a new magnetic phase transition, which has previously not been reported, at $T_{N2} = 11$ K between T_{N1} and T_m . We observed multiple plateaus in the low-temperature magnetic phase and constructed a nontrivial magnetic phase diagram, which results from the competitive interactions in this system. Furthermore, we observed an increase and decrease in the in-plane anisotropy in the transverse magnetoresistance, which is related to the change in the magnetic structure.

DOI: [10.1103/PhysRevMaterials.5.034411](https://doi.org/10.1103/PhysRevMaterials.5.034411)**I. INTRODUCTION**

Chirality, which is a fundamental property of symmetry, plays an important role in many areas of material science. In magnetic compounds with a chiral crystal structure, the Dzyaloshinskii–Moriya (D–M) interaction [1,2] can result in complex magnetic phases such as spin spirals or canted spin structures in molecular-based and inorganic materials [3]. In an interesting example, the emergence of novel topological spin textures has been reported in chiral magnets. A well-known example of an interesting chiral magnet is the B20 chiral compound MnSi, which exhibits a swirling spin texture, called the magnetic skyrmion [4,5]. Another interesting example of a chiral magnet CrNb₃S₆, which is a monoaxial chiral magnet with the space group $P6_322$, exhibits a periodic and nonlinear magnetic order, known as the chiral magnetic soliton lattice [6]. These exotic topological spin states have been observed in several materials [7–9] and have attracted considerable attention for application to novel magnetic memory devices [10–12].

In this study, we focus on a Nd-based monoaxial magnetic compound NdPt₂B. This ternary rare-earth platinum boride belongs to the RPt₂B series ($R =$ rare earth) [13–17] with the hexagonal CePt₂B-type structure of space group $P6_222$ (or $P6_422$), as shown in Fig. 1(a). The magnetic Nd ions form a helical arrangement along the c axis, and the Nd-Pt layers and nonmagnetic boron layers are stacked alternately along the c axis, as shown in Figs. 1(b) and 1(c). Previous studies have investigated the magnetic properties of NdPt₂B using arc-melted polycrystal samples, and it has been reported that NdPt₂B shows an antiferromagnetic transition at approximately 20 K and exhibits a spin flip resulting in a

ferromagnetic phase at approximately 10 K [14]. The RPt₂B series consists of several rare-earth-based isostructural compounds and possesses the same point group D_6 as the typical monoaxial chiral helimagnets CsCuCl₃ and CrNb₃S₆ [19–21]. Therefore the RPt₂B series appears to be an attractive target for investigating chiral magnetism and exotic spin textures. It is noteworthy that rare-earth-based chiral magnets attract interest because of their small characteristic scales of their spin textures [22,23].

In this paper, we report on enantiopure single-crystal growth using the Czochralski method and investigate the magnetic properties of single crystals of Nd-based monoaxial magnetic compound NdPt₂B based on electrical resistivity, specific heat, and magnetization measurements. Magnetization measurements using NdPt₂B single crystals revealed a large magnetic anisotropy. We observed multiple plateaus in the magnetization process in the low-temperature magnetic phase and constructed a magnetic phase diagram. In contrast to a previous report on a polycrystalline sample, the ground state of NdPt₂B is not a simple ferromagnetic phase, as revealed by the magnetic susceptibility and the magnetization measurements. Furthermore, we observed an increase and decrease in the in-plane anisotropy of the transverse magnetoresistance, which is related to a change in the magnetic structure, in the low-temperature magnetic phases. Interestingly, the magnetic susceptibility of enantiopure crystals shows a different behavior to that of the racemic polycrystal, indicating that the D–M interaction plays an important role in the ground state of NdPt₂B.

II. EXPERIMENTAL DETAILS

Single crystals of NdPt₂B were grown using the Czochralski method in a tetra-arc furnace under an argon atmosphere

*yoshi.sato@imr.tohoku.ac.jp

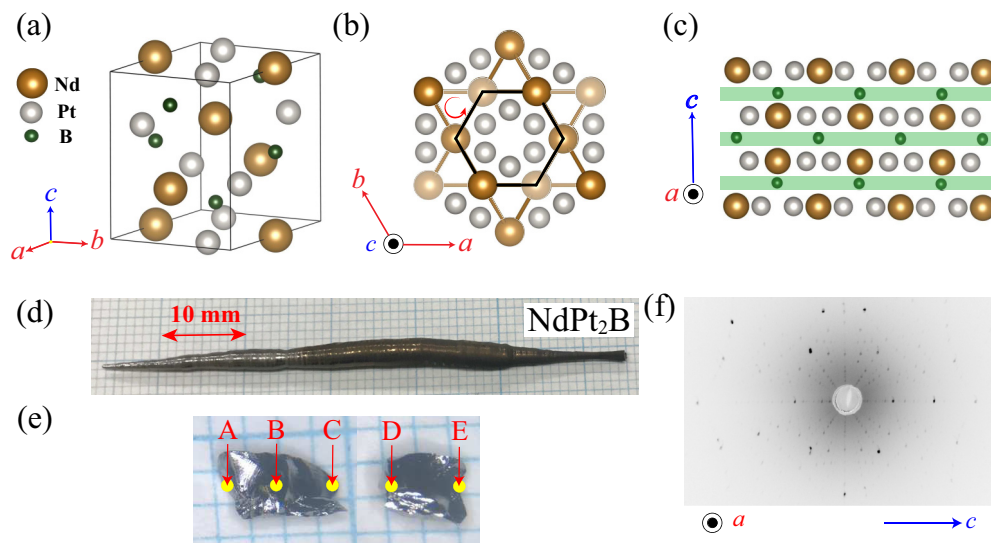


FIG. 1. (a) Unit cell of left-handed (space group: $P6_422$) NdPt_2B . Crystal structures were constructed using the VESTA [18]. (b) Projection of the crystal structure of NdPt_2B on the basal plane. The anticlockwise notation in red indicates the chirality of the Nd atoms. (c) Side view of the crystal structure of NdPt_2B . (d) Grown single crystal of NdPt_2B . (e) Cleaved single crystals of NdPt_2B . The arrows indicate the points measured using single-crystal XRD. (f) Laue photograph of NdPt_2B single crystal.

on a water-cooled copper hearth. The single crystal was pulled from the melting ingot at a speed of 15 mm h^{-1} . The ratio of starting materials was $\text{Nd}:\text{Pt}:\text{B}=1:2:1$. We succeeded in growing NdPt_2B single crystals [refer to Figs. 1(d) and 1(e)] for the first time. In this study, the crystal structure of NdPt_2B single crystals was confirmed using a single-crystal x-ray diffractometer (Rigaku XtaLAB mini II) with a charge-coupled device (CCD) camera and $\text{Mo } K_\alpha$ radiation ($\lambda = 0.71073 \text{ \AA}$). The refined crystal parameters of NdPt_2B are summarized in Tables I and II. The crystal structure was solved using SHELXT [24] and further refined with SHELXL [25]. The homochirality of the NdPt_2B single crystals was confirmed using single-crystal XRD at several points on the specimen, as shown in Fig. 1(e). The Flack parameter is a factor used for estimating the absolute structure of noncentrosymmetric crystal structures. As shown in Table III, the obtained Flack parameters were nearly zero at several points of the NdPt_2B single crystal, indicating the successful growth of the enantiopure crystals with the space group $P6_422$. Note that the arc-melted NdPt_2B polycrystal is a racemic mixture of two structural enantiomers with space groups $P6_222$ and $P6_422$.

To confirm the homogeneity of the single crystals of NdPt_2B , x-ray diffraction data of a powdered single crystal were collected at room temperature using a powder x-ray diffractometer (Rigaku RINT2500V) with $\text{Cu } K_\alpha$ radiation ($\lambda = 1.5418 \text{ \AA}$). The crystal structure was solved using direct methods and refined using EXPO2014 [26], as shown in Fig. 2. The obtained lattice parameters are close to the lattice constants obtained from single-crystal XRD. The single crystals were oriented using a Laue camera (Photonic Science Laue x-ray CCD camera) and cut using a spark cutter.

The electrical resistivity and angular dependence of magnetoresistance were measured using a four-probe AC method with a Quantum Design physical property measurement system (PPMS) with ^3He and rotator options at temperatures down to 0.5 K in magnetic fields up to 2 T . The specific heat was measured using a relaxation method in magnetic fields with a PPMS. The magnetic properties were investigated using a commercial SQUID magnetometer (QD MPMS) at temperatures between 300 and 2 K and in magnetic fields up to 5.5 T .

TABLE I. Crystallographic and structure refinement data of NdPt_2B .

Empirical formula	NdPt_2B
Formula weight	545.23
Crystal system	hexagonal
Space group	$P6_422$ (No. 181)
a (\AA)	5.4426(5)
c (\AA)	7.9001(11)
Volume (\AA^3)	202.66(4)
Formula units per cell (Z)	3
Scan type	$\omega - 2\theta$
Number of measured reflections (total)	600
Number of measured reflections (unique)	241
Cut off angle ($2\theta_{\text{max}}$)	65.8°
Goodness of fit	1.095
Flack parameter	$-0.004(19)$
$R1$ ($I > 2.00s(I)$)	0.0200
R (All reflections)	0.0203
$wR2$ (All reflections)	0.0459
Max Shift/Error	0.000

TABLE II. Atomic positions of NdPt₂B.

NdPt ₂ B				
Atom	Site	x	y	z
Nd	3c	0	0	0
Pt	6i	0.15133(7)	0.30266(7)	0
B	3d	1/2	0	1/2

III. RESULTS

Figure 3(a) shows the temperature dependence of electrical resistivity $\rho(T)$ of the NdPt₂B single crystal for the electrical currents $J \parallel a$ and $J \parallel c$ in a zero field. $\rho(T)$ shows a metallic behavior from room temperature to the lowest temperature, as shown in the inset of Fig. 3(a). Three anomalies were observed in $\rho(T)$ at around $T_m = 9.5$ K, $T_{N2} = 11$ K, and $T_{N1} = 19.5$ K. These results are consistent with those of the specific heat and magnetization measurements, which will be discussed later. In a previous study, only two magnetic transitions were reported at $T = 10$ and 18 K [14], which are similar to the T_m and T_{N1} values determined in this work. $\rho(T)$ decreases upon cooling below T_{N1} for $J \parallel a$, while it increases at T_{N1} for $J \parallel c$. In the low-temperature region in the ordered state, $\rho(T)$ does not follow the T^2 law, namely, $\rho(T) = \rho_0 + AT^2$, where ρ_0 is the residual resistivity. To explain the temperature dependence of the electrical resistivity in the ordered state, we considered the contributions of electronic scattering on the ferromagnetic magnons ρ_{FM} [27] and antiferromagnetic magnons ρ_{AFM} [28]. First, we consider the contribution from ferromagnetic magnons, which can be expressed as follows [27]:

$$\rho_{FM}(T) = c_{FM} T^2 \exp\left(-\frac{\Delta_{FM}}{T}\right), \quad (1)$$

where a coefficient c_{FM} and Δ_{FM} are the material constant and energy gap of the ferromagnetic spin wave, respectively. The fit obtained with the equation $\rho(T) = \rho_0 + AT^2 + \rho_{FM}(T)$ shows a good agreement below $T_m = 9.5$ K, as indicated by the dashed-dotted line in Fig. 3(a). We obtained the parameters $\rho_0 = 14.5 \mu\Omega \text{ cm}$, $A = 4.30 \times 10^{-3} \mu\Omega \text{ cm K}^{-2}$, and $\Delta_{FM} = 18.3$ K.

As we will discuss later, the transition at T_m is not a simple ferromagnetic transition. We also consider the contribution of antiferromagnetic magnons. The magnetic contribution to the electrical resistivity can be written as

TABLE III. Flack parameters of several points on the single crystals of NdPt₂B. The measured points and crystals are shown in Fig. 1(e).

Flack parameter				
A	B	C	D	E
0.01(9)	-0.004(19)	0.03(3)	0.05(3)	0.07(3)

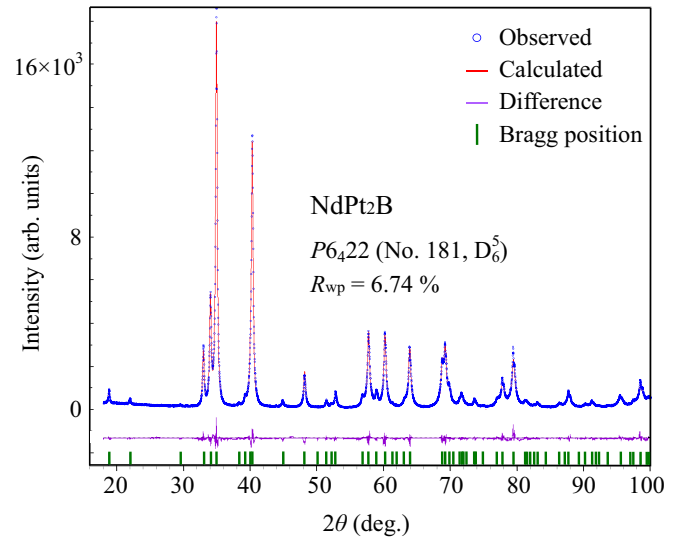


FIG. 2. X-ray diffraction (CuK α) powder pattern of powdered NdPt₂B single crystals. The blue open circles represent the experimental data, while the red solid line is derived from the Rietveld refinement. The purple solid line shows the intensity difference between the experimental data and Rietveld calculations. The estimated background and Bragg peak positions are indicated by the solid green line and bars. R_{wp} is the weighted-profile R factor.

follows [28]:

$$\rho_{AFM}(T) = c_{AFM} \Delta_{AFM}^2 \sqrt{\frac{T}{\Delta_{AFM}}} \exp\left(-\frac{\Delta_{AFM}}{T}\right) \times \left[1 + \frac{2}{3} \left(\frac{\Delta_{AFM}}{T}\right) + \frac{2}{15} \left(\frac{\Delta_{AFM}}{T}\right)^2\right], \quad (2)$$

where the coefficient c_{AFM} is a material constant depending on the spin-wave stiffness, and Δ_{AFM} is the energy gap. The temperature dependence of the electrical resistivity of NdPt₂B can be described by the equation $\rho(T) = \rho_0 + AT^2 + \rho_{AFM}(T)$ below $T_m = 9.5$ K, as indicated by the dashed line in Fig. 3(a), and the residual resistivity ρ_0 , the coefficient A , and the energy gap Δ are estimated to be $\rho_0 = 14.5 \mu\Omega \text{ cm}$, $A = 5.10 \times 10^{-3} \mu\Omega \text{ cm K}^{-2}$, and $\Delta_{AFM} = 30.4$ K, respectively. The energy scale of Δ_{FM} is closer to the transition temperature than that of Δ_{AFM} .

The magnetoresistance $\rho(H)$ exhibits a complex behavior for $J \parallel a$ and magnetic field $H \parallel a$, as shown in Fig. 3(b). Four transitions are observed in $\rho(H)$ at $T = 0.8, 1.7,$ and 5.0 K. At the lowest measurement temperature of 0.5 K, four successive transitions are observed [see Fig. 6(a)]. $\rho(H)$ decreases significantly at approximately $\mu_0 H = 1.5$ T. The decrease in $\rho(H)$ is related to the suppression of magnetic scattering in the polarized state, as reported for several rare-earth antiferromagnets [28–31].

Figure 4(a) shows the temperature dependence of specific heat $C(T)$ in a zero field and in constant magnetic fields of $\mu_0 H = 0.5, 1.0,$ and 1.5 T for $H \parallel a$. The specific heat of NdPt₂B exhibits successive second-order transitions at $T_{N1} = 19.5$ K and $T_{N2} = 11$ K upon cooling. The jump of $C(T)$ at T_{N2} is considerably smaller than that at T_{N1} .

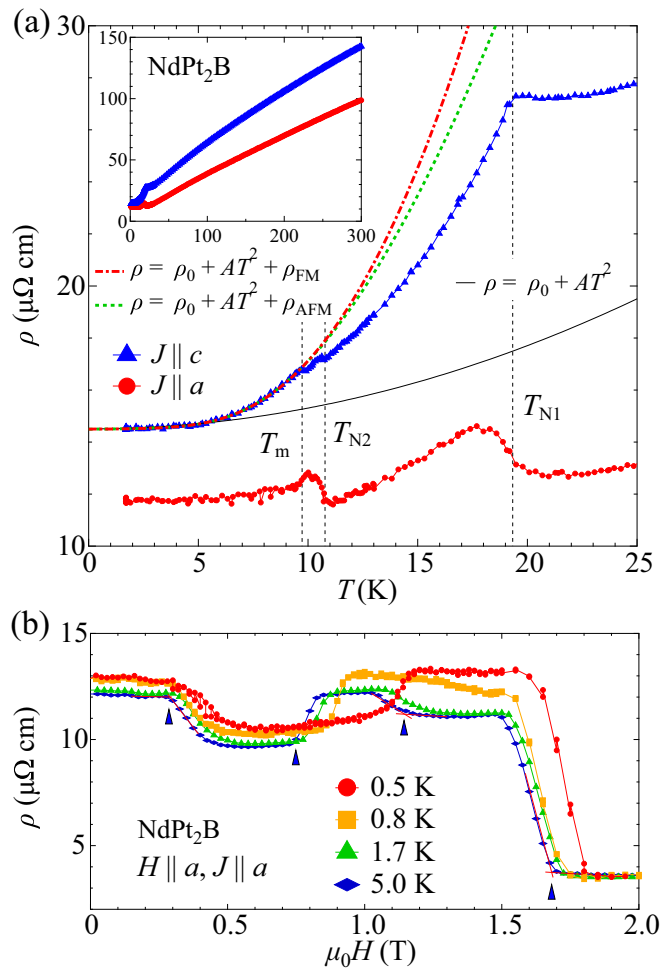


FIG. 3. (a) Temperature dependence of electrical resistivity ρ of the NdPt₂B single crystal for $J \parallel a$ (red circles) and $\parallel c$ (blue triangles) below 25 K. The black solid line corresponds to the curve fitted using the expression $\rho(T) = \rho_0 + AT^2$. The red dashed-dotted and green dashed lines are the curves fitted considering magnetic contributions $\rho_{\text{FM}}(T)$ and $\rho_{\text{AFM}}(T)$, respectively (see text for details). The inset shows the $\rho(T)$ from room temperature to 1.7 K. (b) Field dependence of ρ at $T = 0.5, 0.8, 1.7,$ and 5.0 K up to $\mu_0 H = 2$ T. The anomalies in $\rho(H)$ are indicated by blue arrows for the data measured at 5 K.

Following two second-order transitions, $C(T)$ shows a sharp jump at $T_m = 9.5$ K. In contrast to a previous report [14], the transition appears to have a first-order nature in a zero field. The transition at T_{N2} is rapidly suppressed in a small external magnetic field of 0.2 T, while the transitions at T_{N1} and T_m remain in higher external magnetic fields of approximately 1 T for $H \parallel a$. The first-order transition temperature T_m increases with the magnetic field, while T_{N1} decreases in higher magnetic fields. The second-order transition at T_{N1} and first-order transition at T_m appear to merge at approximately 1.5 T.

Figure 4(b) shows the field dependence of specific heat $C(H)$ at constant temperatures. $C(H)$ of NdPt₂B shows multiple anomalies in the temperature regions below $T_m = 9.5$ K, which are consistent with the magnetoresistance data.

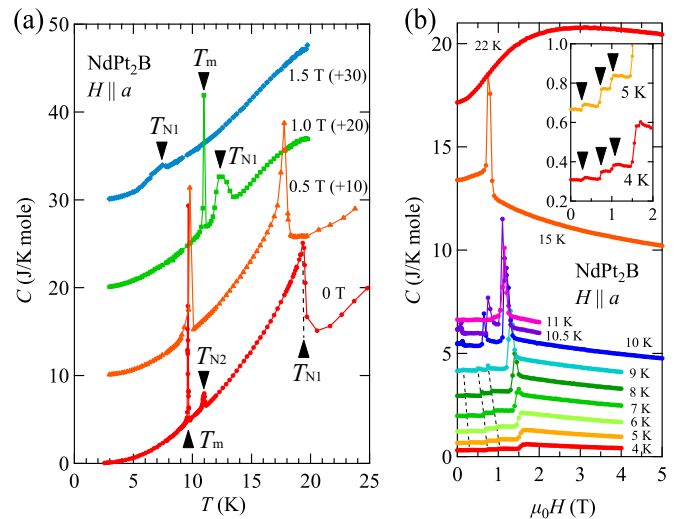


FIG. 4. (a) Temperature dependence of specific heat C in a zero field and in constant magnetic fields of $\mu_0 H = 0.5, 1.0,$ and 1.5 T for $H \parallel a$. The specific heat data are shifted vertically by 10 J/(K mole) for clarity. (b) Field dependence of C measured at various temperatures for $H \parallel a$. The inset shows an enlarged view of C vs. $\mu_0 H$ in the low magnetic field range at $T = 4$ and 5 K.

Moreover, three transitions can be observed in $C(H)$ in the temperature range of $T_m < T < T_{N2}$.

Figure 5(a) shows the magnetization curves of NdPt₂B measured at 2 K for $H \parallel a$, $H \parallel c$, and the $H \perp ac$ plane. The magnetization curves at 2 K clearly indicate strong easy-plane anisotropy. The magnetization starts to saturate with magnetic moments of $2.2 \mu_B/\text{Nd}$ ($H \parallel a$) and $2.0 \mu_B/\text{Nd}$ ($H \perp ac$ plane) at 2 T, while the magnetization continuously increased with increasing fields for $H \parallel c$. The in-plane magnetizations show multiple plateaus at 2 K. To obtain information about the multiple plateaus, we measured the magnetizations at several temperatures. Figure 5(b) shows the magnetization curves at different temperatures and the field derivative of magnetization $dM/d(\mu_0 H)$ at 2 K. As observed in the magnetoresistance and specific heat measurements, $dM/d(\mu_0 H)$ shows four peaks at H_{m1} , H_{m2} , H_{m3} , and H_{m4} in the temperature regions below T_m . Furthermore, three anomalies were observed in the temperature range of $T_m < T < T_{N2}$. A clear hysteresis of each transition was observed between up-sweep and down-sweep at 2 K. The magnetization between H_{m3} and H_{m4} is approximately half the value of the saturated magnetization. Regarding the extra peak at 0.15 T, there was no anomaly in $C(H)$ and $\rho(H)$. Furthermore, no anomaly was observed below H_{m1} in the magnetization curve for the $H \perp ac$ plane.

Figure 5(c) shows the temperature dependence of the zero-field-cooled (ZFC) magnetic susceptibility M/H of NdPt₂B at 0.05 T for $H \parallel a$ and $H \parallel c$. As evidenced by the magnetization, M/H shows large anisotropy with respect to the field direction. M/H shows clear peaks at $T_{N1} = 19.5$ K and $T_{N2} = 11$ K for $H \parallel a$ and $H \parallel c$. Furthermore, M/H increases suddenly at $T_m = 9.5$ K in a magnetic field of 0.05 T for $H \parallel a$ and decreases with the temperature. In contrast, M/H decreases discontinuously at T_m for $H \parallel c$ and increases with a decrease in the temperature. In the

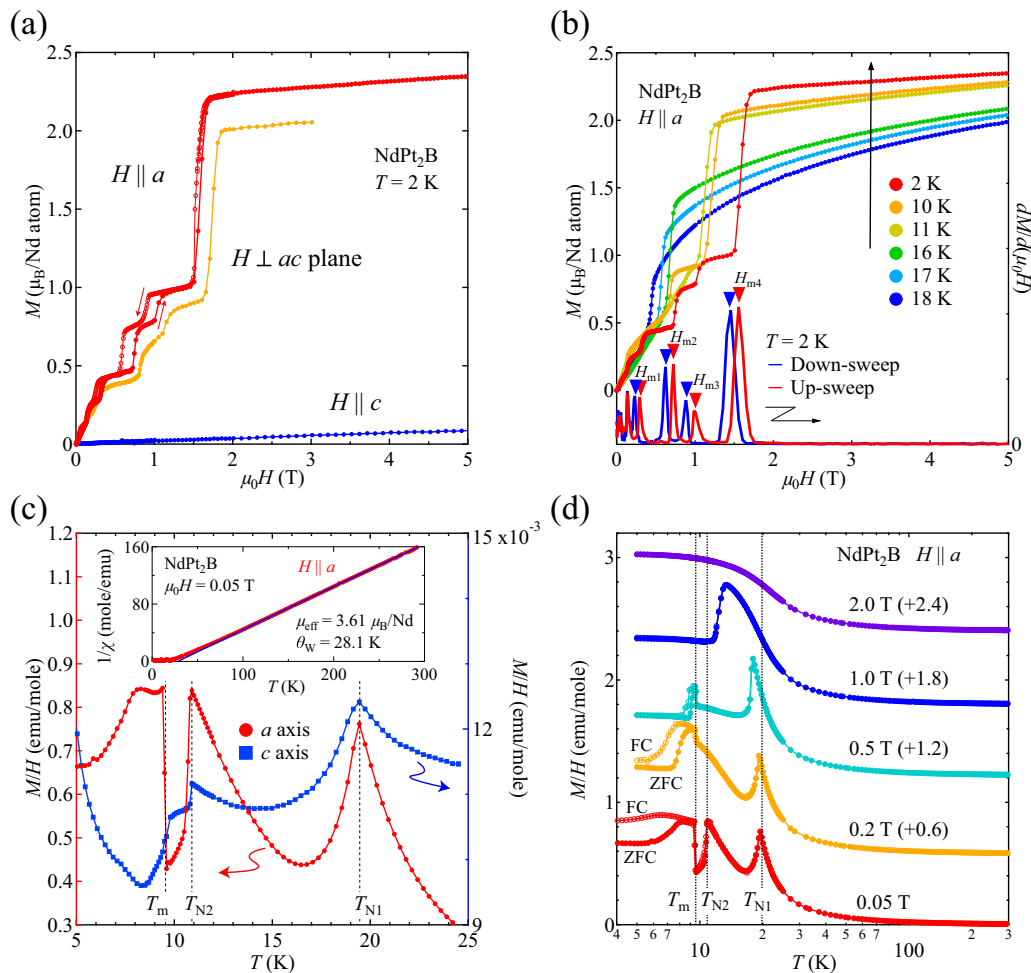


FIG. 5. (a) Magnetization curves of NdPt₂B measured at 2 K for $H \parallel a$ (red), $H \parallel c$ (blue), and the $H \perp ac$ plane (orange). (b) Magnetization curves of NdPt₂B measured at various temperatures for $H \parallel a$ (left axis). The field derivative of magnetization $dM/d(\mu_0 H)$ is also shown on the right axis as a function of the field at 2 K. (c) Temperature dependence of the magnetic susceptibility M/H of NdPt₂B measured at 0.05 T for $H \parallel a$ (red circles, left axis) and $H \parallel c$ (blue squares, right axis) in ZFC condition. The inset shows the temperature dependence of the inverse susceptibility $1/\chi$ for $H \parallel a$. The blue solid line represents a least-squares fit obtained with the modified Curie–Weiss law for NdPt₂B in the paramagnetic region. (d) Magnetic susceptibility M/H of NdPt₂B in different magnetic fields of 0.05, 0.2, 0.5, 1, and 2 T for $H \parallel a$ as a function of the logarithmic temperature. The magnetic susceptibility data are shifted vertically by 0.6 emu/mole.

paramagnetic state, the magnetic susceptibility follows the modified Curie–Weiss law: $M/H = \chi_0 + C_{\text{Curie}}/(T - \theta_W)$ for $H \parallel a$ above 150 K. Here, C_{Curie} and χ_0 are the Curie constant and temperature-independent Pauli-like susceptibility, respectively. The effective magnetic moment μ_{eff} , Weiss temperature θ_W , and χ_0 are estimated to be $\mu_{\text{eff}} = 3.61 \mu_B/\text{Nd}$, $\theta_W = 28.1$ K, and $\chi_0 = 1.70 \times 10^{-4}$ emu/mole, respectively. The obtained μ_{eff} is in reasonable agreement with the theoretical value of $3.62 \mu_B$ of the Nd ion and reported values [14].

Figure 5(d) shows the temperature dependence of the magnetic susceptibility M/H of NdPt₂B in the different magnetic fields of 0.05, 0.2, 0.5, 1, and 2 T for $H \parallel a$. The magnetic susceptibility increases abruptly at T_m for $H \parallel a$, a clear difference between the ZFC and field-cooled (FC) curves at 0.05 T. The difference between the ZFC and FC curves decreases with an increase in the magnetic field and falls to zero at around 1 T.

IV. DISCUSSION

Figures 6(a) and 6(b) show the magnetic (H - T) phase diagrams of NdPt₂B for (a) $H \parallel a$ and (b) the $H \perp ac$ plane obtained from the results for ρ , M , and C under different magnetic fields. As shown in Figs. 6(a) and 6(b), the AFM1 phase and four magnetic phases (MO1, MO2, MO3, and MO4) are separated by the characteristic first-order phase boundary. Furthermore, in the AFM1 phase, a small dome corresponding to the magnetic phase AFM2 exists next to the first-order phase boundary. The AFM2 phase is rapidly suppressed by a small external field. The transition at T_{N2} appears to be related to subtle changes in the magnetic structure. The in-plane H - T phase diagrams are very similar between $H \parallel a$ and the $H \perp ac$ plane, as shown in Figs. 6(a) and 6(b).

The first-order phase boundary at T_m shows a characteristic “S”-shape in the H - T phase diagram, and the MO3 phase

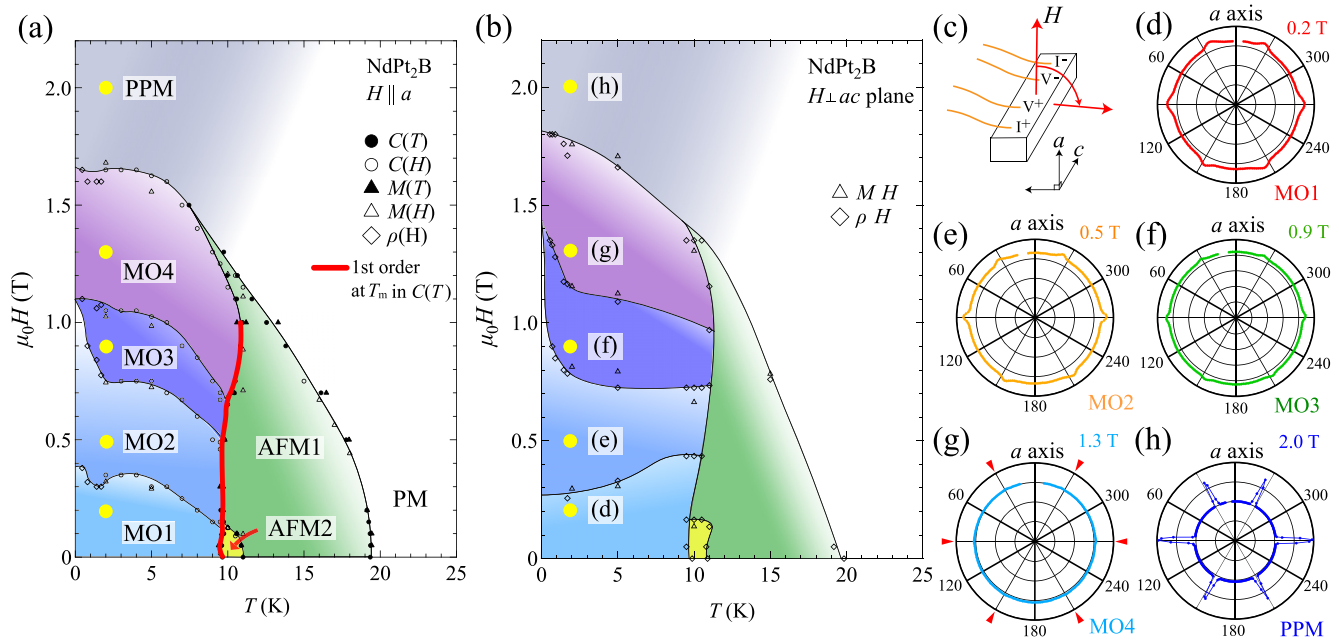


FIG. 6. Magnetic field-temperature phase diagram of NdPt_2B (a) for $H \parallel a$ and (b) the $H \perp ac$ plane. PM, AFM, and PPM correspond to the paramagnetic, antiferromagnetic, and polarized paramagnetic states, respectively. The solid line is guide to the eyes. The red line shows the first-order transition at T_m for $H \parallel a$. (c) Schematic sample configuration for the magnetoresistance measurements. [(d)–(h)] Polar plots of the transverse magnetoresistance for the electrical current $J \parallel c$ in the low-temperature MO and PPM states at 1.7 K. The measurement conditions (T and H) for the transverse magnetoresistance are indicated by yellow markers in the H - T phase diagram of the $H \perp ac$ plane.

exists in a narrow region in the H - T phase diagram at the lowest temperature. The characteristic H - T phase diagram of NdPt_2B is reminiscent of the classical Heisenberg antiferromagnets with triangular lattices [32–34]. In classical Heisenberg antiferromagnets with triangular lattices, the up-up-down-spin (uud) phase exhibits an “S”-shape in the H - T phase diagram, that is, the transition temperature increases in the magnetic field. Furthermore, the uud phase appears only at one specific point at the lowest temperature without thermal fluctuations, which is similar to the behavior of MO3. We consider that it is difficult to describe the crystal structure and spin configurations of NdPt_2B as a simple two-dimensional triangular antiferromagnet. As mentioned in the introduction, however, the magnetic Nd layers are separated by the nonmagnetic boron layers. The two-dimensional magnetic interaction is most likely dominant in the characteristic H - T phase diagram of NdPt_2B .

The multiple plateaus in the magnetization and the corresponding anomalies in $\rho(H)$ and $C(H)$ are observed only below the first-order transition at T_m . On the basis of the above discussion of the phase diagram, the MO1, MO2, MO3, and MO4 phases appear to be related to the change in the in-plane magnetic structure with the two-dimensional magnetic interaction. To obtain information on the change in the in-plane magnetic anisotropy, we performed in-plane transverse magnetoresistance measurements for $J \parallel c$. Figures 6(d)–6(h) show the polar plots of the transverse magnetoresistance in the MO and PPM states measured at 1.7 K. The field-angle dependence of the transverse magnetoresistance exhibits a sixfold symmetry in the ordered state below T_m . The transverse magnetoresistance shows a clear anomaly for the $J \parallel c$ and the $H \perp ac$ plane in the MO1, MO2, and MO3 phases, as shown

in Figs. 6(d)–6(f). However, the anomaly becomes less prominent in the MO4 phase, suggesting a change in the in-plane magnetic structure, as shown in Fig. 6(g). The anisotropy of the in-plane resistivity [$(\rho_{H \perp ac \text{ plane}} - \rho_{H \parallel a}) / \rho_{H \parallel a}$] is approximately 10% in the MO1, MO2, and MO3 phases, while the in-plane anisotropy is less than 1% in the MO4 phase. It should be noted that the sixfold symmetry in the in-plane transverse magnetoresistance is absent in the paramagnetic state at 25 K and 0.5 T. Here, we consider a simple expression for the electrical resistivity: $\rho = \rho_e + \rho_{ph} + \rho_{\text{mag}} + \rho_{\text{FM/AFM}}$, where ρ_e , ρ_{ph} , and ρ_{mag} are the contributions from electron-electron scattering, electron-phonon scattering, and spin-flip scattering (and/or spin-disorder scattering), respectively. Considering the isotropic in-plane transverse magnetoresistance in the paramagnetic state, ρ_e , ρ_{ph} , and ρ_{mag} appear to be isotropic in magnetic fields, and the sixfold symmetry in the transverse magnetoresistance is presumably related to the magnetically ordered state. Hence, the decrease in the in-plane transverse magnetoresistance indicates a change in the magnetically ordered state in MO4. In the PPM state, the transverse magnetoresistance of NdPt_2B shows large anisotropy between $H \parallel a$ and the $H \perp ac$ plane. The in-plane anisotropy is approximately 90% at 2 T in the PPM state.

Here, we discuss the origin of the characteristic first-order transition at T_m . It has been previously reported that the transition at approximately 10 K is a second-order ferromagnetic transition with a spin reorientation [14]; however, our specific heat and magnetic susceptibility measurements indicate the occurrence of the first-order transition at T_m . Furthermore, the magnetization curves below T_m do not appear to be simple ferromagnetic magnetization curves. As shown in

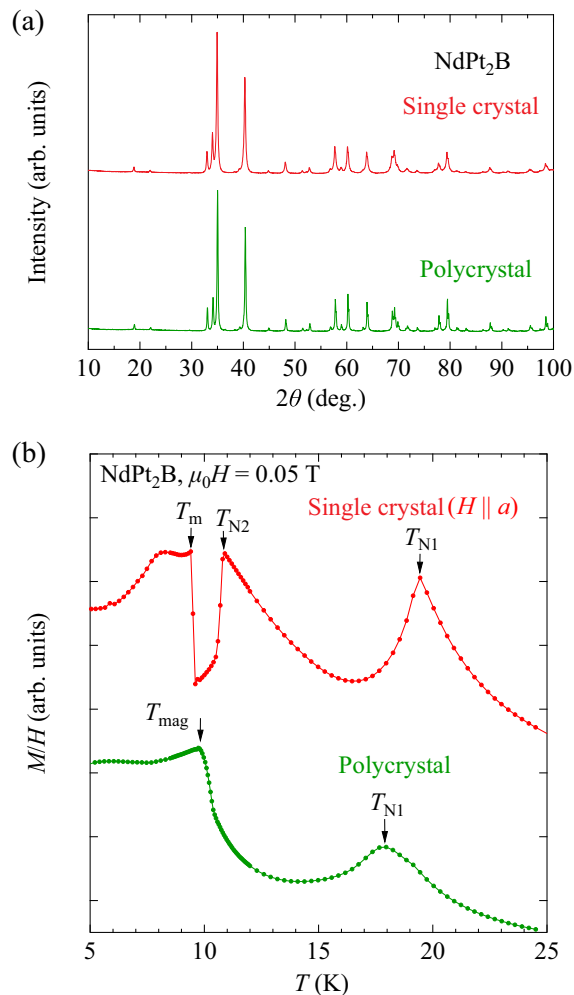


FIG. 7. (a) X-ray diffraction pattern of powdered NdPt₂B single crystals and the polycrystal. (b) Temperature dependence of the magnetic susceptibility M/H of the NdPt₂B single crystal ($H \parallel a$) and polycrystal measured at 0.05 T.

Fig. 5(c), the magnetic susceptibility increases abruptly at T_m in the magnetic field of 0.05 T for $H \parallel a$, while the magnetic susceptibility decreases discontinuously at T_m for $H \parallel c$, indicating that moment reorientation occurs at T_m . The temperature dependence of the magnetic susceptibility at the first-order transition in NdPt₂B is very similar to that of NpRhGa₅ [35]. From neutron diffraction measurements, the first-order transition of NpRhGa₅ is caused by a spin reorientation with different competitive interactions [36]. We inferred that the first-order transition at T_m occurred because of the spin reorientation with competitive interactions, such

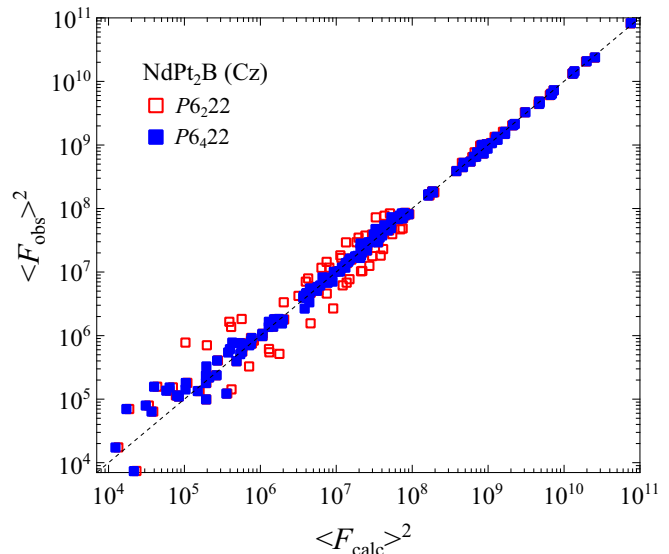


FIG. 8. Plot of observed squared structure factors $\langle F_{\text{obs}} \rangle^2$ of NdPt₂B single crystal as a function of calculated squared structure factors $\langle F_{\text{calc}} \rangle^2$ using logarithmic scale using space groups $P6_22$ (red open squares) and $P6_422$ (blue closed squares).

as ferromagnetic and antiferromagnetic interactions. In fact, the ground state of NdPt₂B does not appear to be a simple ferromagnetic state, but the positive Weiss temperature ($\theta_W = 28.1$ K for $H \parallel a$) indicates that the ferromagnetic interactions are dominant.

In helimagnets with a chiral crystal structure, a fluctuation-induced first-order phase transition has been reported [37–39]. The D–M interaction may be involved in the first-order transition of NdPt₂B. To investigate the role of chirality in the magnetic properties of NdPt₂B, we measured the temperature dependence of the magnetic susceptibility of the enantiopure single-crystalline and racemic polycrystalline sample of NdPt₂B, as shown in Fig. 7(b). Note that the XRD results confirm the single phase of NdPt₂B in both the single-crystalline and polycrystalline samples, as shown in Fig. 7(a). Under a magnetic field perpendicular to the chiral helical axis ($H \parallel c$), $M/H(T)$ shows two second-order transitions along with the first-order transition. In contrast, $M/H(T)$ of the NdPt₂B polycrystal shows two second-order transitions at $T_{N1} = 18$ K and $T_{\text{mag}} = 10$ K, as reported previously [14]. Interestingly, the first-order transition at T_m was only observed in the enantiopure single crystal. We cannot rule out the possibility of the chemical compositions and/or sample dependence being responsible for such a different magnetic behavior. In an interesting example, this greatly differing magnetic behavior between the chiral and racemic samples was reported for a

TABLE IV. Anisotropic displacement parameters of NdPt₂B.

Atom	NdPt ₂ B					
	U_{11}	U_{22}	U_{33}	U_{12}	U_{13}	U_{23}
Nd	0.0052(4)	0.0052(3)	0.0020(4)	0.0026(2)	0	0
Pt	0.0059(2)	0.0059(2)	0.0028(3)	0.00283(18)	−0.00106(14)	−0.00106(14)
B	0.007(6)	0.011(10)	0.012(9)	0.006(5)	0	0

molecule-based magnet [40]. Furthermore, it is noteworthy that the MO2 phase is rapidly enhanced at temperatures below 1 K, as seen in Figs. 3(b), 6(a), and 6(b). This feature in the complex H - T phase diagram has also been observed in other rare-earth monoaxial chiral magnets [41,42]. The enhancement of the MO2 phase at low temperatures in NdPt₂B may be related to the D–M interaction. Further microscopic investigations are necessary to reveal the magnetic structure and role of the D–M interaction. The DM vector, which can be defined under the D–M interaction, is an axial vector that is strongly coupled to the lattice, namely, the right- and left-handed crystal structures. Thus the enantiopure crystal possesses a uniformly aligned DM vector and is suitable for investigating the role of the D–M interaction. As discussed in this paper and previous works [14,17], several magnetic interactions exist in the NdPt₂B and the RPt₂B system. This system provides an attractive platform for examining chiral magnetism and the role of D–M interaction in competitive interactions.

V. CONCLUSIONS

In conclusion, our detailed studies with NdPt₂B enantiopure single crystals revealed nontrivial in-plane H - T phase diagrams and the possible presence of several magnetic interactions such as ferromagnetic, antiferromagnetic, and D–M interactions. In contrast to a previous report, the ground state of NdPt₂B is not a simple ferromagnetic phase, and we reported a new magnetic phase transition at $T_m = 11$ K, as evidenced by the electrical resistivity, specific heat, and magnetization measurements. The magnetization curves and magnetic susceptibility indicate the existence of strong easy-plane anisotropy. We observed an increase and decrease in the sixfold in-plane anisotropy in the transverse magnetoresistance, which is related to the change of magnetic structure in the low-temperature MO phases; however, further microscopic investigations are necessary to reveal the magnetic structure. Interestingly, the characteristic first-order transition at T_m was only observed in the enantiopure single crystal,

suggesting that the D–M interaction is important in understanding the ground state of NdPt₂B.

ACKNOWLEDGMENTS

We would like to thank S. Ohara, Y. Fujima, Y. Yamane, and R. Eguchi for their useful discussions. We thank K. Shirasaki for technical support. We acknowledge all the support from the International Research Center for Nuclear Materials Science at Oarai (IMR, Tohoku University), Laboratory of Alpha-Ray Emitters (IMR, Tohoku University), and Advanced Science Research Center (Japan Atomic Energy Agency). This work was supported by KAKENHI (JP15H05884, JP19H00646), Grant-in-Aid for JSPS Research Fellow (JP19J20539, JP18F18017), and DIARE research grant.

APPENDIX: DETAILS OF SINGLE-CRYSTAL XRD MEASUREMENTS

The measured NdPt₂B single crystal was mounted on a glass fiber. Data were collected at a temperature of 296 K using the ω - 2θ scan. A total of 444 reflections were acquired for the determination of the primitive hexagonal cell, and the 2θ range for cell determination was $8.6^\circ < 2\theta < 66.0^\circ$. An empirical absorption correction and a correction for secondary extinction were applied. The data were corrected for the Lorentz and polarization effects. The crystal structure was determined using direct methods. The structure was successfully refined using anisotropic atomic displacement parameters. Table IV lists the anisotropic displacement parameters for NdPt₂B. A total of 239 independent reflections with $I > 2.00 \sigma(I)$ were acquired, and the R -factors were small enough [$R1 = 2.00\%$ for $I > 2.00 \sigma(I)$ and $wR2 = 4.59\%$].

The final Flack parameter was $-0.004(19)$, indicating that the present absolute structure ($P6_422$) is correct. Figure 8 shows the observed squared structure factors $\langle F_{\text{obs}} \rangle^2$ of the NdPt₂B single crystal as a function of calculated squared structure factors $\langle F_{\text{calc}} \rangle^2$ using space groups $P6_222$ and $P6_422$.

-
- [1] I. Dzyaloshinsky, *J. Phys. Chem. Solids* **4**, 241 (1958).
 [2] T. Moriya, *Phys. Rev.* **120**, 91 (1960).
 [3] Y. Togawa, Y. Kousaka, K. Inoue, and J. Kishine, *J. Phys. Soc. Jpn.* **85**, 112001 (2016).
 [4] S. Mühlbauer, B. Binz, F. Jonietz, C. Pfleiderer, A. Rosch, A. Neubauer, R. Georgii, and P. Bü, *Science* **323**, 915 (2009).
 [5] X. Z. Yu, Y. Onose, N. Kanazawa, J. H. Park, J. H. Han, Y. Matsui, N. Nagaosa, and Y. Tokura, *Nature (London)* **465**, 901 (2010).
 [6] Y. Togawa, T. Koyama, K. Takayanagi, S. Mori, Y. Kousaka, J. Akimitsu, S. Nishihara, K. Inoue, A. S. Ovchinnikov, and J. Kishine, *Phys. Rev. Lett.* **108**, 107202 (2012).
 [7] S. Ohara, S. Fukuta, K. Ohta, H. Kono, T. Yamashita, Y. Matsumoto, and J. Yamaura, *JPS. Conf. Proc.* **3**, 017016 (2014).
 [8] M. Kakihana, D. Aoki, A. Nakamura, F. Honda, M. Nakashima, Y. Amako, S. Nakamura, T. Sakakibara, M. Hedo, T. Nakama, and Y. Ōnuki, *J. Phys. Soc. Jpn.* **87**, 023701 (2018).
 [9] T. Kurumaji, T. Nakajima, M. Hirschberger, A. Kikkawa, Y. Yamasaki, H. Sagayama, H. Nakao, Y. Taguchi, T. Arima, and Y. Tokura, *Science* **365**, 914 (2019).
 [10] J. I. Kishine, I. V. Proskurin, and A. S. Ovchinnikov, *Phys. Rev. Lett.* **107**, 017205 (2011).
 [11] D. A. Gilbert, B. B. Maranville, A. L. Balk, B. J. Kirby, P. Fischer, D. T. Pierce, J. Unguris, J. A. Borchers, and K. Liu, *Nat. Commun.* **16**, 8462 (2015).
 [12] X. Zhang, Y. Zhou, K. M. Song, T.-E. Park, J. Xia, M. Ezawa, X. Liu, W. Zhao, G. Zhao, and S. Woo, *J. Phys.: Condens. Matter.* **32**, 143001 (2020).
 [13] O. L. Sologub, P. Salamakha, H. Noël, M. Potel, M. Almeida, and C. Godart, *J. Alloys. Compd.* **307**, 40 (2000).
 [14] O. L. Sologub, K. Hiebl, and P. S. Salamakha, *Solid State Commun.* **127**, 379 (2003).

- [15] R. Lackner, M. Sieberer, H. Michor, G. Hilscher, E. Bauer, P. S. Salamakha, O. L. Sologub, and K. Hiebl, *J. Phys.: Condens. Matter* **17**, S905 (2005).
- [16] A. B. Shick, J. Kolorenc, J. Ruzs, P. M. Oppeneer, A. I. Lichtenstein, M. I. Katsnelson, and R. Caciuffo, *Phys. Rev. B* **87**, 020505(R) (2013).
- [17] D. Mishra, O. Petravic, A. Devishvili, K. Theis-Bröhl, B. P. Toperverg, and H. Zabel, *J. Phys.: Condens. Matter* **27**, 136001 (2015).
- [18] K. Momma and F. Izumi, *J. Appl. Cryst.* **44**, 1272 (2011).
- [19] Y. Kousaka, H. Ohsumi, T. Komesu, T. Arima, M. Tanaka, S. Sakai, M. Akita, K. Inoue, T. Yokobori, Y. Nakao, E. Kaya, and J. Akimitsu, *J. Phys. Soc. Jpn.* **78**, 123601 (2009).
- [20] A. Miyake, J. Shibuya, M. Akaki, H. Tanaka, and M. Tokunaga, *Phys. Rev. B* **92**, 100406(R) (2015).
- [21] Y. Kousaka, T. Koyama, K. Ohishi, K. Kakurai, V. Hutanu, H. Ohsumi, T. Arima, A. Tokuda, M. Suzuki, N. Kawamura, A. Nakao, T. Hanashima, J. Suzuki, J. Campo, Y. Miyamoto, A. Sera, K. Inoue, and J. Akimitsu, *Phys. Rev. Mater.* **1**, 071402(R) (2017).
- [22] T. Matsumura, Y. Kita, K. Kubo, Y. Yoshikawa, S. Michimura, T. Inami, Y. Kousaka, K. Inoue, and S. Ohara, *J. Phys. Soc. Jpn.* **86**, 124702 (2017).
- [23] M. Kakihana, D. Aoki, A. Nakamura, F. Honda, M. Nakashima, Y. Amako, T. Takeuchi, H. Harima, M. Hedo, T. Nakama, and Y. Ōnuki, *J. Phys. Soc. Jpn.* **88**, 094705 (2019).
- [24] G. M. Sheldrick, *Acta Crystallogr.* **A71**, 3 (2015).
- [25] G. M. Sheldrick, *Acta Crystallogr.* **C71**, 3 (2015).
- [26] A. Altomare, C. Cuocci, C. Giacovazzo, A. Moliterni, R. Rizzi, N. Corriero, and A. Felcicchio, *J. Appl. Cryst.* **46**, 1231 (2013).
- [27] A. R. Mackintosh, *Phys. Lett.* **4**, 140 (1963).
- [28] M. B. Fontes, J. C. Trochez, B. Giordanengo, S. L. Bud'ko, D. R. Sanchez, E. M. Baggio-Saitovitch, and M. A. Continentino, *Phys. Rev. B* **60**, 6781 (1999).
- [29] K. Sengupta and E. V. Sampathkumaran, *J. Phys.: Condens. Matter* **18**, L401 (2006).
- [30] D. Aoki, C. Paulsen, H. Kotegawa, F. Hardy, C. meingast, P. Haen, M. Boukahil, W. Knafo, E. Resoushe, S. Raymond, and J. Flouquet, *J. Phys. Soc. Jpn.* **81**, 034711 (2012).
- [31] Y. J. Sato, Y. Shimizu, A. Nakamura, Y. Homma, D. X. Li, A. Maurya, F. Honda, and D. Aoki, *J. Phys. Soc. Jpn.* **87**, 074701 (2019).
- [32] M. V. Gvozdikova, P.-E. Melchy, and M. E. Zhitomirsky, *J. Phys.: Condens. Matter* **23**, 164209 (2011).
- [33] L. Seabra, T. Momoi, P. Sindzingre, and N. Shannon, *Phys. Rev. B* **84**, 214418 (2011).
- [34] M. Lee, E. S. Choi, X. Huang, J. Ma, C. R. Dela Cruz, M. Matsuda, W. Tian, Z. L. Dun, S. Dong, and H. D. Zhou, *Phys. Rev. B* **90**, 224402 (2014).
- [35] D. Aoki, Y. Homma, Y. Shiokawa, H. Sakai, E. Yamamoto, A. Nakamura, Y. Haga, R. Settai, and Y. Ōnuki, *J. Phys. Soc. Jpn.* **74**, 2323 (2005).
- [36] S. Jonen, N. Metoki, F. Honda, K. Kaneko, E. Yamamoto, Y. Haga, D. Aoki, Y. Homma, Y. Shiokawa, and Y. Ōnuki, *Phys. Rev. B* **74**, 144412 (2006).
- [37] M. Janoschek, M. Garst, A. Bauer, P. Krautscheid, R. Georgii, P. Böni, and C. Pfleiderer, *Phys. Rev. B* **87**, 134407 (2013).
- [38] D. G. Franco, Y. Prots, C. Geibel, and S. Seiro, *Phys. Rev. B* **96**, 014401 (2017).
- [39] Y. Homma, M. Kakihana, Y. Tokunaga, M. Yogi, M. Nakashima, A. Nakamura, Y. Shimizu, A. Maurya, Y. J. Sato, F. Honda, D. Aoki, Y. Amako, M. Hedo, T. Nakama, and Y. Ōnuki, *J. Phys. Soc. Jpn.* **88**, 094702 (2019).
- [40] H. Higashikawa, K. Okuda, J. Kishine, N. Masuhara, and K. Inoue, *Chem. Lett.* **36**, 1022 (2007).
- [41] H. Ninomiya, Y. Matsumoto, S. Nakamura, Y. Kono, S. Kittaka, T. Sakakibara, K. Inoue, and S. Ohara, *J. Phys. Soc. Jpn.* **86**, 124704 (2017).
- [42] I. Ishii, K. Takezawa, T. Mizuno, S. Kumano, T. Suzuki, H. Ninomiya, K. Mitsumoto, K. Umeo, S. Nakamura, and S. Ohara, *Phys. Rev. B* **99**, 075156 (2019).